PAPER

Check for updates

Novel gamma-irradiated chitosan-doped reduced graphene-CuInS₂ composites as counter electrodes for dye-sensitized solar cells†

Yonrapach Areerob,[a] Chaowalit Hamontree,[a] Phitchan Sricharoen, [iD] [b] Nunticha Limchoowong, [iD] [c] Sakchai Laksee,[d] Won-Chun Oh [iD] [ef] and Kongsak Pattarith [iD] *[g]

To address the issues associated with traditional counter electrodes, a novel gamma-irradiated chitosan-doped reduced graphene-CuInS₂ composite (Chi@RGO-CIS) was used as the counter electrode (CE). The system was fabricated following a simple hydrothermal method. The prepared Chi@RGO-CIS was characterized by various spectroscopic and microscopic techniques. The synergistic effect between chitosan, CuInS₂, and reduced graphene oxide can help in producing a large surface area. It can also help in the generation of catalytic sites toward I-/I₃-redox electrolytes. We used a composite (based on electrical considerations) to study the effect of the amount of graphene on the characteristics and photovoltaic efficiency of the Chi@RGO-CIS composites. The solar cell assembled with 1.5% Chi@RGO-CIS exhibited an efficiency of 12.21%. The efficiency was higher than that of a Pt-based device (9.96%) fabricated under the same conditions. Hence, Chi@RGO-CIS can be potentially used as the CE of dye-sensitized solar cells (DSSCs). It can be used as a substitute for Pt in DSSCs.

1   Introduction

Dye-sensitized solar cells (DSSCs) are promising inexpensive photovoltaic devices that can be used for converting solar energy to electrical energy. They are easy to fabricate and cost-effective. Thus, their use is preferred over traditional silicon-based solar cells.[1] Typically, the components of a DSSC include a TiO₂ mesoporous thin film sensitized (Photoanode, PE) with N719 dye molecules, an electrolyte of iodide/triiodide (I⁻/I₃⁻), and a counter electrode (CE).[2] When the DSSCs are irradiated with light, the dye molecules reach their excited state. The electrons in the excited state immediately move toward the semiconductor conduction band (CB) from the lowest-unoccupied-molecular-orbital (LUMO) of the dye molecules. Electrons from the surface of the mesoporous (TiO₂) semiconductor move toward the CE through an external circuit. After excitation, the dye molecules become electron deficient.

The electrolyte then transfers electrons to the photosensitizer and diffuses toward the CE, where the reduction reaction occurs.[3,4] The most used CE material is platinum (Pt), as it is characterized by good conductivity, chemical stability, inertness, and excellent catalytic activity.[5] However, a significant amount of Pt is required to fabricate DSSCs on a commercial scale, and this limits the practical application of the process as Pt is not readily available. There are several other drawbacks of using Pt. This metal is expensive, corrodes in the presence of an electrolyte, and is ineffective for function in the electrolyte of the iodine-free redox couple.[6] As a result, other CEs are considered alternatives to Pt for carrying out the reduction reactions.

Recently, there have been several interesting studies on the application of quantum dots owing to their many outstanding properties. CuInS₂ (CIS) is a ternary metal sulfide and belongs to a group of nanomaterials known as semiconductor fluorescent nanoparticles or quantum dots (QDs).[7] It has unique advantages, such as high quantum yield, good photochemical stability, a long fluorescence lifetime, a wide absorption spectrum and a narrow emission spectrum, tunable size, resistance to photobleaching, large surface area, and low cost. Moreover, it can absorb light in the visible spectrum, showing fluorescence

[a]*Department of Industrial Engineering, School of Engineering, King Mongkut's Institute of Technology Ladkrabang, Bangkok 10520, Thailand*

[b]*Department of Premedical Science, Faculty of Medicine, Bangkokthonburi University, Thawi Watthana, Bangkok 10170, Thailand*

[c]*Department of Chemistry, Faculty of Science, Srinakharinwirot University, Bangkok 10110, Thailand*

[d]*Nuclear Technology Research and Development Center, Thailand Institute of Nuclear Technology (Public Organization), Nakhon Nayok 26120, Thailand*

[e]*College of Materials Science and Engineering, Anhui University of Science & Technology, Huainan, 232001, PR China*

[f]*Department of Advanced Materials Science & Engineering, Hanseo University, Seosan-si, Chungcheongnam-do, 31962, South Korea*

[g]*Department of Chemistry, Faculty of Science, Buriram Rajabhat University, Buriram 31000, Thailand*

† Electronic supplementary information (ESI) available. See https://doi.org/10.1039/d2ra01749k

emissions in the visible and near-infrared region and a direct bandwidth of about 4.5 eV. However, it has many QDs that can be used for DSSC cells. The main materials used in QDs are CdS, CdSe, CdTe, ZnSe, PbS, PbSe, and InP. In 2019, U. Mehmood and A. Haq Khan[8] used a simple fabrication method of low-cost lead sulfide (PbS) as a counter electrode in DSSC. PbS showed a power-conversion-efficiency (PCE) of 4.71%, which is still low for DSSC applications. Therefore, CIS QDs have attracted considerable attention in the field of materials for DSSC cells.

Chitosan, a natural biopolymer composed of β-1,4-linked 2-acetamido-D-glucose and β-1,4-linked 2-amino-D-glucose, is the deacetylated derivative of chitin. Chitosan has attracted immense attention as a functional biopolymer as it is widely used in the food, agriculture, and medical industry. It is also attributed to its good biodegradability, film-forming properties, inexpensive, and environmentally friendly.[9,10] The physicochemical and functional properties of chitosan are usually dependent on molecular weight (M_w). It has been reported that the solubility, growth-promoting properties, and electrical properties of low-M_w chitosan are substantially better than those of high-M_w chitosan.[11] Normally, chitosan can be degraded under conditions of acidic and alkaline hydrolysis. It can also be degraded under conditions of enzymatic treatment. The M_w can be effectively reduced under these conditions. However, the major problems associated with these reactions include long processing time, high processing cost, low yield, and generation of toxic chemical waste. To address these problems, the process of irradiation is used. It is an eco-friendly approach and is thus preferred over conventional techniques. Gamma irradiation has been productively used to degrade polysaccharides such as starch, cellulose, and chitosan.[12] Gamma irradiation reduces the M_w of chitosan and improves the physicochemical, electrical properties, and structure of the system via chain scission, crosslinking, and breaking of bonds. The interactions of the hydroxyl and the amino groups in chitosan play important roles in enhancing the electrical properties of the system under study.[13]

Graphene, a two-dimensional carbon nanomaterial, has attracted immense interest as it can be used to fabricate photocatalysts and sensors. It can also be used for energy conversion and storage as it exhibits low resistance, excellent optical transmittance, high mechanical stability, and high chemical stability.[14] Furthermore, the hybrid nanocomposite materials based on graphene can be used to improve the power conversion efficiency of the DSSC cells significantly. This can be attributed to the synergistic relationship between graphene and other metal oxide nanostructures.[15] Recently, graphene (based on composite materials) has been used to improve the efficiency of the DSSC cells. Tamilselvi and co-workers[16] designed a NiSe$_2$/graphene hybrid following a facile one-step hydrothermal method. The power conversion efficiency (PCE) reported by them was approximately 10.6% for a NiSe$_2$/graphene CE, and it was higher than that achieved using bare NiSe$_2$ CE (6.04%) under the same conditions.

As a result, to improve the DSSC cell efficiency, we created a novel gamma-irradiated chitosan-doped reduced graphene-CuInS$_2$ composite (Chi@RGO-CIS) that can function as a CE.

This nanomaterial was created using a straightforward hydrothermal method. The optimum proportion of graphene in the composite was determined to improve the PCE. This also helped in fabricating a good electro-catalyst. The charge transfer efficiency and stability could also be increased. The device fabricated with 1% Chi@RGO-CIS exhibited a PCE of 12.21%. The efficiency was comparable to the efficiency of conventional Pt-based DSSCs.

2 Experimental procedures

2.1 Chemicals and materials

Graphite flakes, sodium nitrate (NaNO$_3$), potassium permanganate (KMnO$_4$), sulfuric acid (H$_2$SO$_4$, 98%), and hydrogen peroxide (H$_2$O$_2$, 30%) were purchased from Sigma Aldrich, Thailand. Ethylene glycol, In(NO$_3$)·6H$_2$O (>99%), Cu(NO$_3$)·3H$_2$O (>99%), iodine, N719 dye, and fluorine-doped tin oxide (FTO)-coated glass slides sheet resistance ~7 Ω sq^{-1} were purchased from Sigma Aldrich. All the other chemicals used in the experiments were of analytical grade.

2.2 Synthesis of gamma-irradiated chitosan doped graphene-CuInS$_2$ composites

Graphene oxide (GO) was synthesized following a modified Hummer's method.[17] Graphite powder (10 g) was added to 100 mL of concentrated H$_2$SO$_4$ under magnetic stirring conditions. The mixture was stirred continuously for 1 h at 0 °C. Following this, 30 g of KMnO$_4$ was added to the graphite solution. The resulting mixture was stirred at 25 °C for 2 h. Following the addition of the reagent, the solution was heated to 100 °C. Subsequently, 50 mL of H$_2$O$_2$ solution was added dropwise to the above solution under magnetic stirring conditions. The reagent was added for 3 h. Finally, the solution was subjected to conditions of suction filtration, and the powder thus obtained was washed repeatedly with absolute ethanol and deionized water. Following this, the powder was placed in an oven at 80 °C and dried for 2 h to obtain graphene.

The CuInS$_2$ catalyst was synthesized following a simple hydrothermal.[18] Equimolar solutions of copper chloride (0.01065 g) and indium chloride (0.0553 g) were mixed with sodium citrate and glutathione in ethylene glycol under conditions of stirring (30 min). Following this, 0.5 g of graphene powder and 1.0 g of gamma-irradiated chitosan were added to the solution. This mixed solution was transferred to a 150 mL Teflon-coated stainless-steel autoclave and heated at 180 °C for 8 h in an air oven. The catalyst obtained after the reaction was washed five times using pure ethanol and DI water. To obtain the gamma-irradiated chitosan-doped graphene-CuInS$_2$ composites, the catalyst was placed in an air oven at 80 °C overnight (CGCs). Fig. 1 depicts the schematic diagram of the synthetic process.

2.3 DSSC assembly

The Chi@RGO-CIS composite-based CE and TiO$_2$ photoanode (with I$^-$/I$_3^-$ pairs of liquid electrolytes) were sandwiched following the doctor blade method. The RGO content in
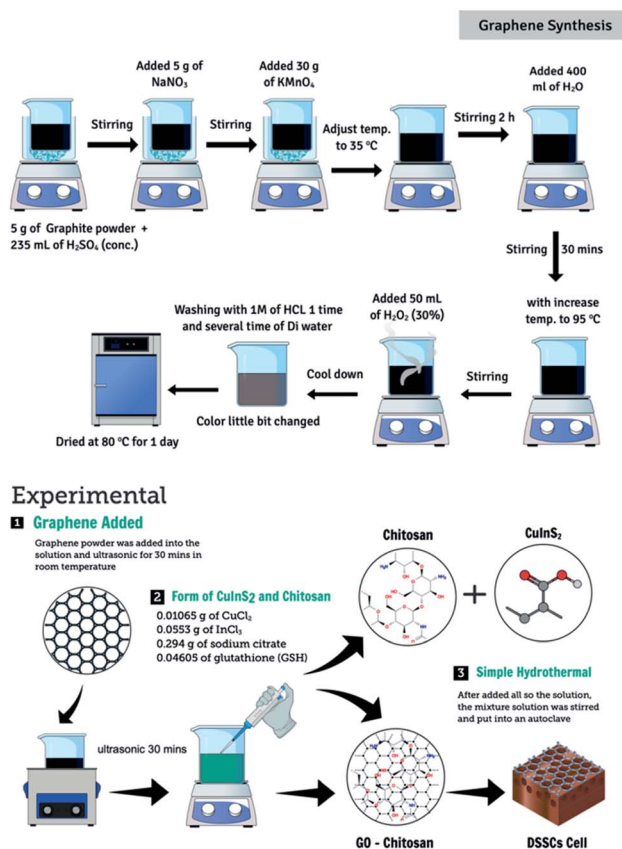
Fig. 1 Schematic diagram of the CGC synthesis procedure.

Chi@RGO-CIS was varied as 1%, 1.5%, and 2%. Two layers were used to prepare the TiO_2 paste on the FTO substrates. Following this, the samples were annealed at a temperature of 450 °C for 30 min. Following this, the TiO_2 paste on the FTO glass was soaked in a ruthenium (N719) solution (soaking time: 24 h). The Chi@RGO-CIS catalyst-based CE was deposited following a spin coating technique using the FTO substrate. Surlyn film (approximately 30 μm) was used to clip the TiO_2 photoanode and the Chi@RGO-CIS catalyst-based CE with each other. This helped form a sandwich-type cell. The Pt-based DSSCs were manufactured to equate the electrodes formed by the replacement of Chi@RGO-CIS with the Pt-based CE.

2.4 Characterization

The X-ray diffraction (XRD) technique was used to determine the phase composition of the developed palladium oxide. The experiments were conducted using a Rigaku, SmartLab Model. The field emission scanning electron microscopy (FE-SEM, Apreo 2, Thermo Fisher Scientific, Germany) technique was used to record the scanning electron microscopy images. The images were analyzed to determine the morphology of the Chi@RGO-CIS composites. Photocurrent–voltage (J–V) characterization of the DSSCs were carried out under one sun conditions (100 mW cm^{-2}, AM 1.5 G) using a source meter (Keithley 2440) and a class AAA solar simulator. The electrochemical

impedance spectroscopy (EIS) technique characterized the samples in the frequency range of 0.01–100 kHz at 0 V bias.

3 Results and discussion

3.1 Structural properties and morphology

3.1.1 XRD analysis. The crystallographic phases of the synthesized Chi@RGO-CIS catalysts were analyzed using the XRD technique. Fig. 2 presents the XRD patterns of (a) RGO, (b) chitosan after gamma irradiation, and (c) Chi@RGO-CIS. The board diffraction peak at 26.02° corresponds to the crystalline (002) plane associated with RGO.[19] For the $CuInS_2$ (CIS) spectra indicated the diffraction peaks at 18.02°, 22.21°, 24.38° and 26.11° which can be indexed to the (100), (002), (101) and (110) planes of $CuInS_2$ (JCPDS card file no. 85-1575) respectively. The diffraction peaks corresponding to the chitosan after irradiation-based nanocomposite appeared at approximately 14.11° and 18.72°. This indicated a hydrated crystalline structure. The broad peak at approximately 22.15° indicates an amorphous structure of chitosan.[20] The peaks corresponding to $CuInS_2$ appeared at 29.1°, 31.4°,[1–32] 42.5°, and 49.1° for the planes (112), (200), (204), and (312), respectively. This indicated the complete conversion of In_2S_3 into $CuInS_2$. Analysis of the XRD patterns also reveals that the resulting $CuInS_2$ is characterized by a tetragonal crystal structure (JCPDS card no. 75-0106). Under gamma-irradiation, the intensity of the peaks increased, the specific peaks narrowed, and the peaks became sharper in the case of the Chi@RGO-CIS nanocomposite.

3.1.2 Morphology of the composite. The morphology and microstructure of the prepared Chi@RGO-CIS composite were characterized using the TEM and FE-SEM techniques. The results are shown in Fig. 3 and 4. The graphene sheet, $CuInS_2$ (CIS), chitosan, and Chi@RGO-CIS were analyzed using the FE-SEM technique, as shown in Fig. 3(a–d). The FE-SEM image of graphene shows the presence of 2D ultrathin nanosheets (Fig. 3(a)). The images reveal that the $CuInS_2$ composite exhibited irregular shape and rough surface. It was observed that these exhibited unique 3D micro-spherical structures and
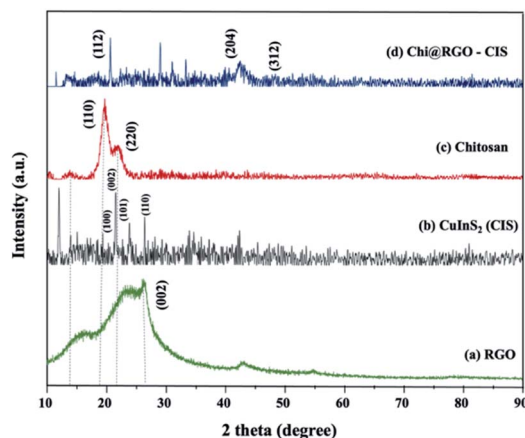

Fig. 2 X-ray diffraction (XRD) patterns recorded for (a) RGO, (b) irradiated chitosan, and (c) Chi@RGO-CIS.
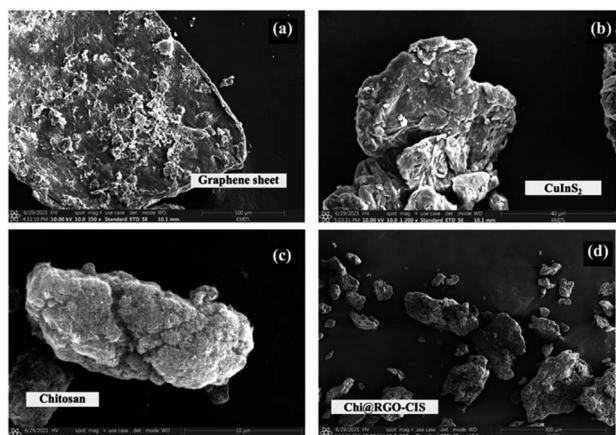
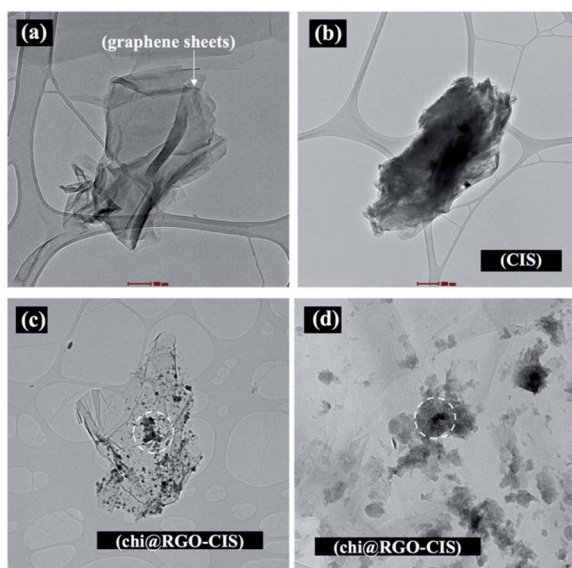Fig. 3 SEM images recorded for (a) RGO sheets and (b and c) Chi@RGO-CIS.

Fig. 4 TEM images recorded for (a) RGO sheets and (b and c) Chi@RGO-CIS.

were characterized by a rough surface (Fig. 3(b)). The average diameter of the CIS structures was estimated to be approximately 40 μm. The chitosan appears fluffy and is characterized by a rough texture. The average diameter was approximately 10 μm (Fig. 2(c)). The Chi@RGO-CIS composite appeared as a combination of particles and amorphous structures. The diameter was approximately 300 μm. The special structure integrates the advantages of nanostructures and microstructures, resulting in increased surface area of the composite.

Chi@RGO-CIS TEM images were captured to study the morphology of the RGO sheets. The TEM images of the RGO sheets are shown in Fig. 4(a). The thicknesses of the sheets are depicted in the figures. The black dots observed in the images recorded for Chi@RGO-CIS represented chitosan and CIS (average size: approximately 10–20 nm). These were present on

the surface of graphene sheets. The results confirmed the good crystallinity of the novel composite.[21]

3.1.3 FTIR and Raman spectra. The FTIR spectral profiles of RGO and Chi@RGO-CIS are presented in Fig. 5. The spectral profile recorded for GO shows the presence of peaks at approximately 1066 cm^{-1}. This peak was attributed to C–O stretching. The peak at 1288 cm^{-1} was attributed to C–O–C bending. The peak corresponding to C–OH bending appeared at 1577 cm^{-1}. The peak at 1720 cm^{-1} corresponded to the C=O stretching vibration. The broad peak at 3445 cm^{-1} was attributed to the stretching vibrations of the O–H group present in the C–OH groups and water. The broadband at approximately 3290 cm^{-1} was attributed to the overlap of the peak corresponding to the axial stretching vibrations of the hydroxyl groups (O–H) and the peaks corresponding to the asymmetric/symmetric stretching of the amine bonds (N–H). The band observed at 2867 cm^{-1} was attributed to axial stretching of the –C–H group in the chitosan chain. The band centered at 1587 cm^{-1} corresponds to the bending vibration of the primary amine (NH_2) in the polymeric chitosan chain. Peaks corresponding to other functional moieties (polysaccharide ring or end groups) in chitosan were also observed. The peak corresponding to C–N stretching appeared at 1418 cm^{-1}, the peak corresponding to CH_3 bending appeared at 1372 cm^{-1}, and the peak corresponding to C–OH stretching appeared at 1025 cm^{-1}. Analysis of the FTIR spectral profile indicated the successful modification of chitosan in the Chi@RGO-CIS composite.[22–25]

Using Raman spectroscopy, the structural quality of RGO and Chi@RGO-CIS was investigated (Fig. 6). The two peaks at around 1350 cm^{-1} were assigned to the D band (A1 g breathing mode), and the peak at 1560 cm^{-1} was assigned to the G band (symmetric E_{2g} of sp^2 carbon atoms) of graphene (blue line).[26] Moreover, the chitosan polymer matrix depicts peaks at 1150 cm^{-1}, 1250 cm^{-1} can be assigned as the following: the C–C stretching region and the main peak at 2815 cm^{-1}. Which are related to the stretching vibration of activated hydrogen and C–H saturated methylene, respectively. While the profile
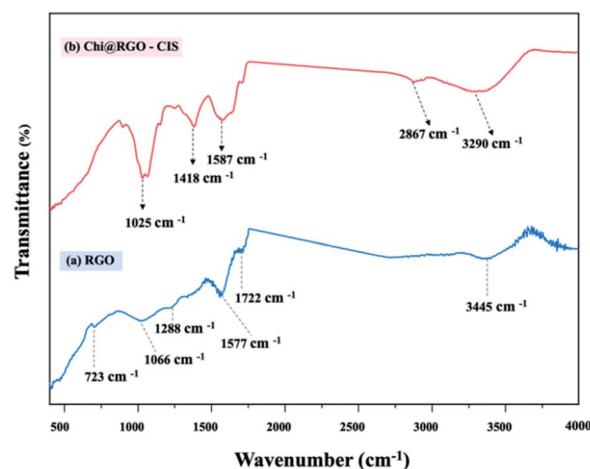

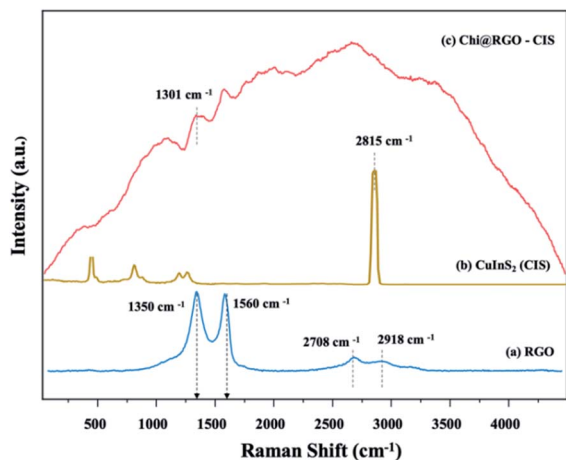Fig. 5 FTIR spectral profiles recorded for (a) RGO and (b) Chi@RGO-CIS.

Fig. 6 Raman spectral profiles recorded for (a) RGO and (b) Chi@RGO-CIS.

corresponding to powdered Chi@RGO-CIS is shown in Fig. 6 (red line). Five peaks appear at 240, 263, 291, 319, and 340 cm^{-1}, and these were assigned to the E, B2, A1, E, and B2 modes of the chalcopyrite phase of CuInS$_2$. The strong peak appearing at 291 cm^{-1} can be potentially assigned to the A1 mode, while the

peak at 340 cm^{-1} can be assigned to the B2 mode. Overall, an almost similar spectrum trend was observed in chitosan/ graphene oxide (Chi/GO) nanohybrid with some shifts in bands position. It consists of the vibrations of chitosan and RGO, which confirms the blending of chitosan with RGO. The peak at 1301 cm^{-1} between chitosan and RGO through hydrogen bonding. Moreover, the peaks of chitosan decreased, which means less active hydrogen and more methylene groups after crosslinking. Chitosan also states that the reason for the decrease in peak at 2815 cm^{-1}.

3.1.4 Chemical states of Chi@RGO-CIS. The X-ray photoelectron spectroscopy (XPS) technique was used to investigate further the chemical composition of the prepared Chi@RGO-CIS Fig. 7(a–e). Analysis of the XPS profiles presented in Fig. 7(a) confirms the presence of Cu, In, and S (for CIS) in the resulting Chi@RGO-CIS composites. The peak at 284.6 eV was ascribed to the sp^2 hybridized C–C bond, while the peak at 285.7 eV corresponded to the sp^3 hybridized C–C bond. The peak at 286.6 eV was attributed to the C–O bond, and the peak at 289.0 eV was ascribed to the O–C =O bond (Fig. 7(b)). The high-resolution O 1s spectrum, presented in Fig. 7(c), shows the presence of three intense peaks at 529.5, 531.2, and 533.1 eV. These peaks were ascribed to the lattice oxygen in RGO.[27] The characteristic peaks of N 2p at the binding energies of 399.0 eV, 401.2 eV, and 403.2 eV, correspond to the –N–H, O=C–N, and
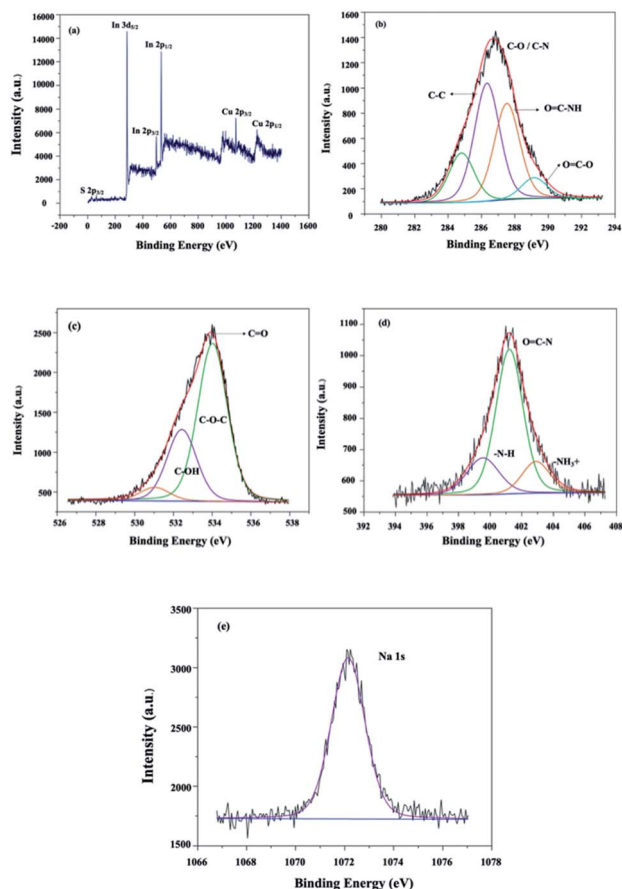

Fig. 7 XPS profiles recorded (a) under conditions of high-resolution, (b) for C 1s, (c) for O 1s, (d) for N 2p, and (e) for Na 1s.
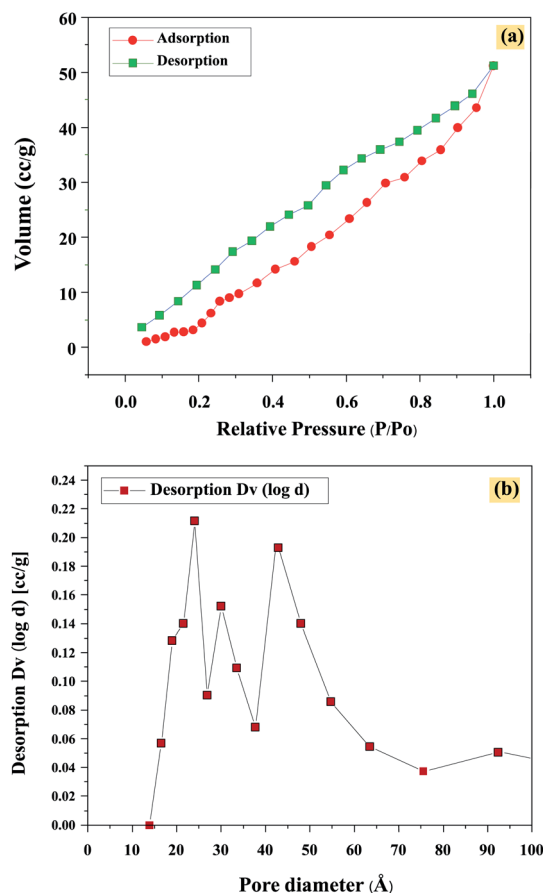

Fig. 8 (a) Isotherm and (b) pore size of Chi@RGO-CIS.

Table 1 Photovoltaic performance of Chi@RGO-CIS CE under conditions of varying RGO contents

Sample	V_{oc} (V)	J_{sc} (A cm^{-2})	FF	PCE (%)	R_s (Ω)	R_{ct} (Ω)
Pt electrode	0.78	19.16	0.66	9.96	10.78	71.43
1.0% Chi@RGO-CIS	0.81	18.43	0.58	8.82	10.32	40.32
1.5% Chi@RGO-CIS	0.86	22.70	0.62	12.21	10.21	31.12
2.0% Chi@RGO-CIS	0.79	14.90	0.54	6.83	10.88	128.7

$-NH^{3+}$ units (Fig. 7(d)). The sodium functionalities could be identified by analyzing the Na 1s profiles. The peak at a binding energy of 1072.0 eV confirmed the oxidation state of the chitosan unit after gamma irradiation.[28]

3.1.5 N$_2$ adsorption–desorption properties. The N$_2$ adsorption–desorption isotherms, pore size distribution, and specific area of Chi@RGO-CIS are presented in Fig. 8(a). The Chi@RGO-CIS samples present a mode of type I, suggesting that they are primarily characterized by a micro-porous structure. The high BET surface area (3.41 m^2 g^{-1}; pore volume: 0.0127 mL g^{-1}) could be attributed to the high surface area of chitosan and RGO coated on CIS. In addition, the average pore size of Chi@RGO-CIS was in the range of 20–50 nm (Fig. 8(b)). The highly porous nanostructures and large BET surface area impart the Chi@RGO-CIS electrode with excellent reactivity in the presence of electrolytes and active materials. It also allows the establishment of rapid charge transfer kinetics.[28]

3.2 Electrochemical measurements

3.2.1 Photovoltaic (PV) study with DSSCs. The PV characteristics of each cell were measured under AM 1.5 G simulated sunlight. The current density–voltage (J–V) characteristics of DSSCs are shown in Fig. 9. The obtained photovoltaic parameters are presented in Table 1, and the overall efficiencies were calculated as follows:

$$\eta = (J_{SC} \times V_{OC} \times FF)/P_{Light} \tag{1}$$

As the photon-to-current conversion efficiency (η) depends on the open-circuit photovoltage (V_{OC}), short circuit photocurrent density (J_{SC}), and fill factor (FF). The Pt-based CE exhibited a PCE of approximately 9.96% ($V_{OC} = 0.78$ V, $J_{SC} = 19.16$ mA cm^{-2}, FF = 0.66). The maximum PCE recorded for the 1.5% Chi@RGO-CIS system was 12.21% (under similar conditions). The enhanced performance can be attributed to the synergism between the increased surface area available for electrolyte reduction and the increased conductive path between the chitosan CIS nanoparticles realized following the addition of RGO. However, the PCE recorded for 2% Chi@RGO-CIS (6.83%) decreased with an increase in the concentration of RGO. This may be attributed to the formation of impure crystals or the presence of an excess of precursor materials with CIS crystals. These impurities act as trapping sites and severely block the movement of electrons. Under these conditions, the current density (J_{SC}) decreases at higher contents.[29]

3.2.2 EIS analysis. The EIS technique was used to determine the interface resistance and study the kinetics of charge transport for Chi@RGO-CIS at the CEs/electrolyte interface.[30] The Nyquist plots generated for the Pt-based DSSC Pt electrode, 1% Chi@RGO-CIS, 1.5% Chi@RGO-CIS, and 2% Chi@RGO-CIS
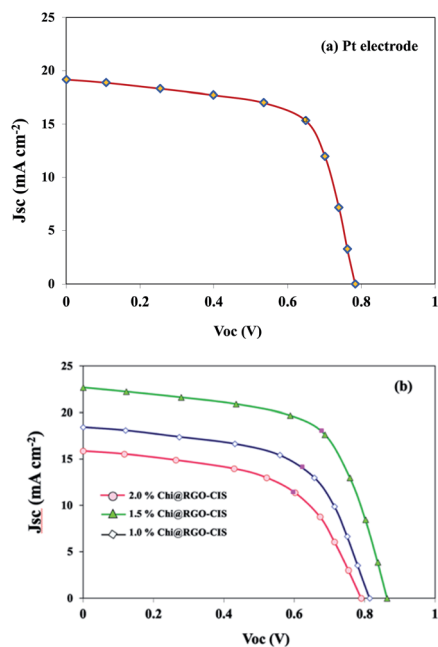

Fig. 9 Current–voltage characteristics of DSSCs fabricated using Pt, 1.0% Chi@RGO-CIS, 1.5% Chi@RGO-CIS, and 2% Chi@RGO-CIS.
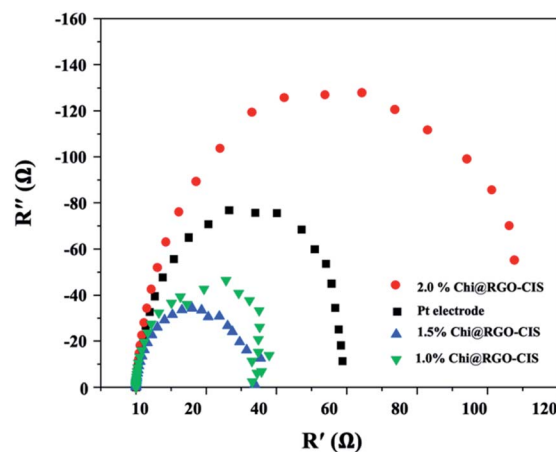

Fig. 10 Nyquist plots generated using the electrochemical impedance spectroscopy (EIS) technique for Pt, 1.0% Chi@RGO-CIS, 1.5% Chi@RGO-CIS, and 2% Chi@RGO-CIS.

CEs are presented in Fig. 10, and the results are listed in Table 1. It normally comprises of three semicircles. The first semicircle denotes the charge transfer resistance (R_{ct}) at the interface of CE and the electrolyte. The charge transfer resistance (R_s) at the interface of the electrolyte and the photoanode is represented by the second arc. The third arc shows the diffusion of the redox couple in the electrolyte (Zw). The magnitude of interface resistance depends on the diameter of the semicircles. The results reveal that the DSSCs fabricated with 1.5% Chi@RGO-CIS CE exhibit slightly lower R_{ct} (value: 32.04 Ω) than the DSSCs fabricated using Pt-based cells (value: 72.33 Ω). This indicates that an increased electrocatalytic ability for I_3 reduction can be achieved using 1.5% of Chi@RGO-CIS. The increase in activity can be attributed to the occurrence of the rapid charge-transfer process.[31,32]

4 Conclusions

By optimizing the amounts of RGO, we were able to successfully fabricate the Chi@RGO-CIS composite-based CE for the fabrication of DSSCs. The synthesized Chi@RGO-CIS composite is electrochemically stable, exhibits high catalytic activity, possesses a large surface area, and contains a large number of electrocatalytic sites that are utilized for reduction reactions taking place at counter electrodes. The maximum PCE recorded for DSSCs fabricated using 1.5% Chi@RGO-CIS was 12.21%. This was higher than the PCE (recorded under the same conditions) of Pt-based DSSCs (9.96%). The excellent performance achieved using Chi@RGO-CIS could be attributed to the excellent electrocatalytic activity of the system toward the I^-/I_3^- redox reaction. The conditions of gamma irradiation help in obtaining a large surface area. Many electrocatalytic sites (for CIS) are also generated under these conditions. These results suggested that cubical Chi@RGO-CIS nanocrystals could be the best alternative catalyst for Pt-free DSSCs.

Author contributions

Y. Areerob, C. Hamontree and S. Laksee conceived and planned the experiments. Y. Areerob and C. Hamontree carried out the experiment. Y. Areerob wrote the manuscript with support from K. Pattarith and W.C. Oh. P. Sricharoen and N. Limchoowong verified the analytical methods. All authors discussed the results and contributed to the final manuscript.

Conflicts of interest

There are no conflicts to declare.

Acknowledgements

Notes and references

1 D. K. Shah, D. KC, T. G. Kim, M. S. Akhtar, C. Y. Kim and O. B. Yang, *Opt. Mater.*, 2021, **121**, 111500.

2 D. S. Patil, K. C. Avhad and N. Sekar, *Comput. Theor. Chem.*, 2018, **1138**, 75–83.

3 E. Demir, A. Savk, B. Sen and F. Sen, *Nano-Struct. Nano-Objects*, 2017, **12**, 41–45.

4 K. Ahmad, A. Mohammad and S. M. Mobin, *Electrochim. Acta*, 2017, **252**, 549–557.

5 B. S. Arslan, S. N. Ülüş, M. Gezgin, B. Arkan, E. Güzel, D. Avcı, M. Nebioğlu and İ. Şişman, *Opt. Mater.*, 2020, **106**, 109974.

6 R. Singh, N. Kaur, Navjyoti and A. Mahajan, *Sol. Energy*, 2021, **226**, 31–39.

7 F. Gao, K. Liu, C. Ruzhou and Y. Zhang, *Appl. Surf. Sci.*, 2020, **528**, 146560.

8 U. Mehmood and A. Khan, *Sol. Energy*, 2019, **193**, 1–5.

9 Z. Jiang, K. Zhang, L. Du, Z. Cheng, T. Zhang, J. Ding, W. Li, B. Xu and M. Zhu, *Mater. Sci. Eng., C*, 2021, **126**, 112178.

10 V. C. Dumont, H. S. Mansur, A. A. P. Mansur, S. M. Carvalho, N. S. V. Capanema and B. R. Barrioni, *Int. J. Biol. Macromol.*, 2016, **93**, 1465–1478.

11 A. A. Varghese, E. Kuriakose, J. Jose, S. Aryal, R. Khanal and E. Anila, *Appl. Surf. Sci.*, 2022, **579**, 152162.

12 N. G. Madian and N. Mohamed, *J. Mater. Res. Technol.*, 2020, **9**(6), 12970–12975.

13 T. A. Dar, M. Uddin, M. Masroor, A. Khan, A. Ali, S. R. Mir and L. Varshney, *J. Radiat. Res. Appl. Sci.*, 2015, **8**(3), 446–458.

14 I. Bano, M. A. Ghauri, T. Yasin, Q. Huang and A. D. Palaparthi, *Int. J. Biol. Macromol.*, 2014, **65**, 81–88.

15 K. Olszowska, J. Pang, P. S. Wrobel, L. Zhao, H. Q. Ta, Z. Liu, B. Trzebicka, A. Bachmatiuk and M. H. Rummeli, *Synth. Met.*, 2017, **234**, 53–85.

16 R. Kaur, K. H. Kim and A. Deep, *Appl. Surf. Sci.*, 2017, **396**, 1303–1309.

17 C. Tamilselvi, P. Duraisamy and N. Subathra, *Diamond Relat. Mater.*, 2021, **116**, 108396.

18 A. Alkhouzaam, H. Qiblawey, M. Khraisheh and M. Atieh, *Ceram. Int.*, 2020, **46**(15), 23997–24007.

19 M. Ali, J. E. Nady, S. Ebrahim and M. Soliman, *Opt. Mater.*, 2018, **86**, 545–549.

20 T. Soltani, A. Tayyebi and B. K. Lee, *Sol. Energy Mater. Sol. Cells*, 2018, **185**, 325–332.

21 A. M. Zardkhoshoui and S. S. H. Davarani, *J. Electroanal. Chem.*, 2018, **827**, 221–229.

22 Z. Luan, Y. Tian, L. Gai, H. Jiang, X. Guo and Y. Yang, *J. Alloys Compd.*, 2017, **729**, 9–18.

23 H. Alijani, M. Abdouss and H. Khataei, *Diamond Relat. Mater.*, 2022, **122**, 108817.

24 J. Singh and A. S. Dhaliwal, *J. Phys. Chem. Solids*, 2022, **160**, 110358.

25 O. C. Olatunde and D. C. Onwudiwe, *Results Chem.*, 2022, 100273.

26 W. Wei, L. Wang, Q. Huang and T. Li, *J. Alloys Compd.*, 2019, **783**, 37–43.

27 L. Sun, J. Sun, K. Zhang, X. Sun, S. Bai, Y. Zhao, R. Luo, D. Li and A. Chen, *Sens. Actuators, B*, 2022, **354**, 131194.

28 B. Huang, Z. Zhang, N. Ding, Y. Zhuang, G. Zhang and P. Fei, *Int. J. Biol. Macromol.*, 2022, **194**, 246–253.

29 M. Alhaddad and A. Shawky, *J. Mol. Liq.*, 2020, **318**, 114377.

30 A. Das, R. R. Wary and R. G. Nair, *Solid State Sci.*, 2020, **104**, 106290.

31 S. Shital, S. K. Swami, P. Barnes, V. Dutta and M. Carlo, *Sol. Energy*, 2018, **161**, 64–73.

32 H. Y. Chen, B. Y. Huang, H. S. Koo and M. T. Huang, *Optik*, 2020, **220**, 164899.